Tellus
SERIES A DYNAMIC METEOROLOGY AND OCEANOGRAPHY
PUBLISHED BY THE INTERNATIONAL METEOROLOGICAL INSTITUTE IN STOCKHOLM

Tellus (2008), 60A, 679–687
Printed in Singapore. All rights reserved

TELLUS

Structure of the precipitable water field over Mount Etna

By MIN ZHU[1], GEOFF WADGE[1*], RACHEL J. HOLLEY[1], IAN N. JAMES[2], PETER A. CLARK[3], CHANGGUI WANG[3] and MARGARET J. WOODAGE[1], [1]*Environmental Systems Science Centre, University of Reading, Reading RG6 6AL, U. K.;* [2]*Department of Meteorology, University of Reading, Reading RG6 6BB, U. K.;* [3]*Joint Centre for Mesoscale Meteorology, Met Office, Reading RG6 6BB, U. K.*

(Manuscript received 4 May 2007; in final form 8 January 2008)

ABSTRACT

The structure of the precipitable water (PW) field over mountains is difficult to observe and can have a complex form. We demonstrate a method to analyse this structure with a case study at the Etna volcano in Sicily. The method involves decomposition of the PW field, power spectral analysis and high-resolution numerical modelling including an experiment to show the sensitivity to solar radiative forcing which can drive the mesoscale circulations and consequently the complex patterns of water vapour advection in complex terrain near a coastline. The PW decomposition and power spectral analysis were applied to both the model data and remotely sensed MODIS data. The PW field has two structural components: a horizontal mean component and a horizontal perturbation component that possesses a wave number $k$dependence of $k^{-\frac{5}{3}}$ in the mesoscale range. For our case example (summer, mid-morning) we show that the horizontally perturbed component is largely driven by the combined land-sea and upslope breeze effects.

1. Introduction

The spatial structure of precipitable water (PW) in the atmosphere is a key component of forecasting weather and climate change (Trenberth et al., 2005; Kuo et al., 1996). Over the past decade significant progress has been made in PW observation and modelling through the use of remote sensing instruments, space-borne radiometers and global positioning system (GPS), as well as high-resolution numerical models. Nevertheless, such structure can be particularly difficult to interpret in mountains because of the complex nature of the PW field, as a result of the interactions between the orography, vegetation and the multiscale atmospheric system. For example, Wadge et al. (2002) showed that for a high Froude number case, the moist air is advected up the upwind slope and an intrusion of dry air descended the lee side of the mountain. The lee side of mountains generally show a more complex flow pattern and variable water vapour field. Numerical experiments by Rotunno and Ferretti (2001) showed that orographically modified flow was a critical element for the production of extraordinary rainfall. In order to improve our understandings of observed and modelled PW structure genesis and evolution over mountains, we need an effective way to help analyse the multiscale PW field.

*Corresponding author:
e-mail: gw@mail.nerc-essc.ac.uk
DOI: 10.1111/j.1600-0870.2008.00317.x

Knowledge of the atmospheric PW field is also needed to mitigate the radio wave propagation delay caused by tropospheric water vapour in the Differential Interferometric Synthetic Aperture Radar (DInSAR) technique. The water vapour effect is the largest single source of error for the DInSAR technique (Massonnet and Feigl, 1998). Therefore accuracy of measurements of surface deformation by this technique over areas such as volcanoes and earthquake ruptures can be greatly improved by such knowledge. For example, Remy et al. (2003) showed that the interferometric phase differences due to the variable PW field over the Sakurajima volcano (Japan) could be modelled by a calibrated, non-linear variation with altitude. However, the structure of the PW field can contain not just a component due to the exponential distribution of PW with altitude (Foster and Bevis, 2003), but also one due to the lateral dynamic behaviour of the atmosphere as it moves around and over mountains. In particular, the effect that the land-sea breeze effect has on advecting water vapour and producing a distinct radio wave propagation effect measured by DInSAR. In this paper, we propose a method utilizing satellite remote sensing data (Moderate Resolution Imaging Spectroradiometer [MODIS]-retrieved PW) and a high-resolution forward atmospheric model (the U. K. Meteorological Office Unified Model [UM]) to analyse these two components of the atmospheric PW structure over mountains. We decompose the PW field into a horizontal mean PW field evaluated at the surface pressure and a horizontal perturbation component. The numerical model helps us to interpret the formation of the perturbed water vapour over mountains. We chose the 3300 m-high Mount Etna volcano in Sicily to test the method. Although the volcano is not strictly axisymmetric, its quasi-conical shape is similar to the bell-shaped circular mountains with large-amplitude used in most theoretical studies (Miranda and James, 1992; Baines, 1995). Section 2 describes the method in detail, section 3 analyses the results and section 4 discusses the findings.

2. Method

We have chosen a cloud-free day, 27 July 2005, as a case study. Our model data are sampled at 1030 coordinated universal time (UTC), the time of acquisition of MODIS data, and close to the time at which satellite radars often acquire their data for InSAR studies.

2.1. MODIS data processing

MODIS is an imaging radiometer on NASA's Terra and Aqua satellites, that can acquire data with global coverage every 3 d. Five near-IR channels in the 0.8–1.3 μm range (three water vapour absorption and two non-absorption channels) are used by MODIS to retrieve the vertically integrated PW field. The theoretical accuracy of the MODIS PW product is claimed to be 5–10% over land, much less over water, and hence we only use on-land MODIS values for analysis. Li et al. (2005) found a satisfactory correlation among MODIS-, radiosonde- and GPS-derived PW fields. We processed MODIS data in the following steps: (1) geolocate the data; (2) mask areas contaminated by cloud at the 95% confidence level; (3) mask the areas near coasts. The processed MODIS data that we used have a sample spacing of approximately 2.5 km $\times$ 2.5 km over the Etna area. Figure 1 shows the MODIS sampling points over Etna mountain at 1020 UTC 27 July 2005. For the purpose of performing the PW decomposition for MODIS data, a digital elevation model with 1 arc second resolution ($\sim$30 m) was used to estimate the surface elevation at the MODIS sampling locations. The dataset is a combination of Shuttle Radar Topography Mission (SRTM) data with 3 arc second resolution ($\sim$90 m) and topographic information derived from 1 arc second resolution European Remote Sensing satellite (ERS) tandem mission InSAR data (Fig. 1).

2.2. Atmospheric modelling

The model used is the atmospheric module of the UM, version 5.5 (Met Office, 2004). The UM is a non-hydrostatic, deep atmospheric, grid point model with an Arakawa-C grid in the horizontal plane and a terrain-following Charney–Philips grid in the vertical plane. The main variables are the three components of wind, potential temperature, Exner pressure, density and components of moisture (vapour, cloud water and cloud ice). Model physics includes land surface (vegetation cover type, soil temperature and moisture) and planetary boundary layer (PBL) processes, radiation, cloud microphysics and convection. For our particular purpose, the model is run in a nested mode with cell sizes of 60 km, 12 km, 4 km and 1 km respectively and with 38 vertical layers (13 layers within the PBL). The outermost domain (60 km) is global. The innermost domain (1 km) covers the whole of Sicily. The orography at the 1 km scale uses the Global One-km Base Elevation (GLOBE) model, http://www.ngdc.noaa.gov/seg/topo/globe.shtml). A semi-implicit, semi-Lagrangian and predictor-corrector algorithm is used for model integration. The time step for the 1 km domain is 30 seconds and the lateral boundary conditions for the 1 km domain are interpolated from the 4 km domain every 15 minutes. The model was initialized at 0600 UTC 27 July

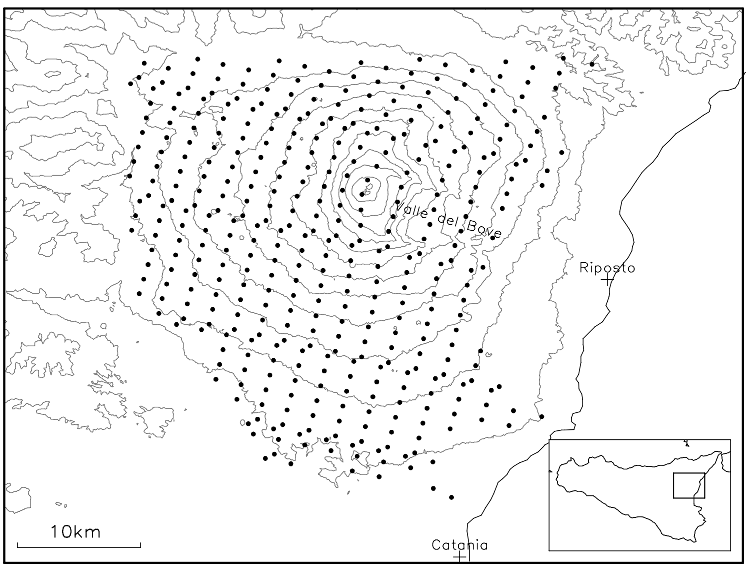

Fig. 1. Map of the orography of Etna (contour interval 250 m) showing the moderate resolution imaging spectroradiometer (MODIS) precipitable water (PW) sampling points (black dots) at 1020 UTC 27 July 2005.

2005 with the European Centre for Medium-Range Weather Forecasts (ECMWF) global atmospheric analysis (0.5 ° latitude × 0.5° longitude) and run for a 6-hour period, with output at a 15-minute frequency. MODIS data were acquired at 1020 UTC. We also performed a sensitivity experiment by running the UM model without the solar radiation scheme (hereafter NSR), comparing the results to those obtained from the forecast with the scheme running (hereafter CTL). The modelled PW fields are interpolated and registered onto MODIS data locations for comparison. Validation of the use of the UM in modelling water vapour over Mount Etna was presented by Zhu et al. (2007).

2.3. PW field decomposition

There are two components to the water vapour spatial variability, $q(x, y, p)$, where q is the specific humidity and x, y, p are the three-dimensional co-ordinates. The first is vertical variability, assuming no horizontal heterogeneities ($\bar{q}^{xy}(p)$, $-^{xy}$ denotes area average). The second is horizontal variability, resulting partly from turbulent processes in the atmosphere ($q'(x, y, p)$). We illustrate how the above two components of humidity lead to decomposition of the PW field through the following symbolic derivations:

$$q(x, y, p) = \bar{q}^{xy}(p) + q'(x, y, p) \quad (1)$$

$$PW(x, y) = \frac{1}{g}\int_{p_s(x,y)}^{p_t} q(x, y, p)dp \quad (2)$$

$$\bar{P}\bar{W}(x, y) = \frac{1}{g}\int_{p_s(x,y)}^{p_t} \bar{q}^{xy}(p)dp \quad (3)$$

$$PW'(x, y) = \frac{1}{g}\int_{p_s(x,y)}^{p_t} q'(x, y, p)dp \quad (4)$$

$$PW(x, y) = \bar{P}\bar{W}(x, y) + PW'(x, y) \quad (5)$$

in which PW, $\bar{P}\bar{W}$, PW' are the full PW, horizontal mean PW field evaluated at the surface pressure (hereafter the horizontal mean component) and the PW horizontal perturbation component respectively, p_s and p_t are the pressure at the Earth's surface and the top of the atmosphere respectively and g is gravitational acceleration.

Practically, we separate these two components using knowledge of the orography. We plot the observed and modelled PW values for 27 July 2005 against their corresponding surface elevations in Fig. 2. Foster and Bevis (2003) analysed the distribution of PW from several GPS sites over Hawaii and found an exponential relationship between the PW and the surface elevation. Here, we use a quadratic function to fit the data. Fitting such a function is a good approximation to the operation in eq. (3), and the curves in Fig. 2 represent the relationship between the horizontal mean component of observed/modelled PW and the surface elevation. Given both the air density and specific humidity decreasing exponentially with increasing surface elevation in eq. (3), it is not difficult to explain the exponential decrease behaviour of horizontal mean component of PW with surface elevation in Fig. 2. We define the observed/modelled horizontal perturbation PW field to comprise the departure of the full field from the corresponding quadratic regression curve in Fig. 2 (see eq. (5)).

2.4. Power spectral analysis

The behaviour of the horizontal perturbation component of the PW field can be described mathematically using several interrelated measures, such as the power spectrum, the covariance

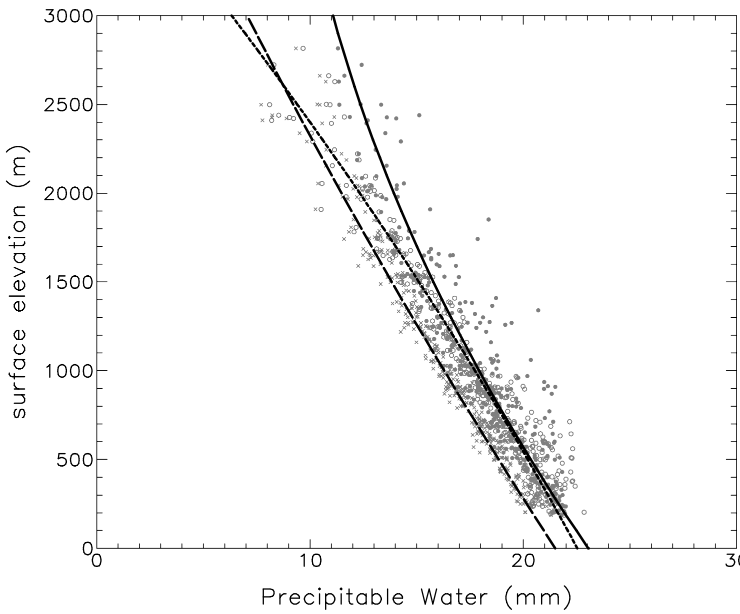

Fig. 2. Scatterplot of observed (closed circle) and modelled (CTL: open circle, NSR: cross) PW versus surface elevation over Etna mountain at 1020 UTC 27 July 2005. Best fitting curves have the form of $PW = a + b \cdot z + c \cdot z^2$, where z is surface elevation. For MODIS (solid curve): $a = 23.05\ mm$, $b = -5.69 \times 10^{-3}\ mm/m$, $c = 5.67 \times 10^{-7}\ mm/m^2$; CTL (short dashed curve): $a = 22.53\ mm$, $b = -4.49 \times 10^{-3}\ mm/m$, $c = -3.02 \times 10^{-7}\ mm/m^2$; NSR (long dashed curve): $a = 21.49 mm$, $b = -5.39 \times 10^{-3}\ mm/m$, $c = 1.93 \times 10^{-7}\ mm/m^2$.

function, the structure function and the fractal dimension. We choose the power spectrum for analysis, which has the advantage of demonstrating the observed/modelled spatial structure of moisture at different scales (Hanssen, 2001). In order to avoid the difficulty in computing spectra in 2D non-periodic domains, we followed Skamarock's 1D kinetic energy spectrum calculation method (Skamarock, 2004). In this, we compute a 1D spectrum by averaging 1D spectral energy densities of the horizontal perturbation component PW field computed along the ranges perpendicular to the satellite track. Skamarock (2004) showed that the spectra computed in this way are comparable with those derived from the 1D observational data, and the 1D non-periodic problem can be largely alleviated by using a detrending technique and increasing the sample of individual spectra. We selected 24 rows each 27.5 km long and neglected other data samples. This can largely avoid the noise problem induced by the non-uniform length of the sample series. We note that non-equally spaced rows of points can distort the spectrum, in particular at short wavelengths (Avara and Kays 1971). We compared the surface elevation spectrum from MODIS sample points with that from the Unified Model 1 km grid and found that the spectrum from the MODIS sample points is generally reasonable at wavelengths greater than 10 km (see Fig. 5d).

3. Results

We now present an analysis of the structures of the observed and modelled PW fields over Etna on 27 July 2005 after applying the PW and power spectra decompositions. We validate the model using MODIS data and interpret the mechanism of formation of PW field components using the sensitivity experiment results.

3.1. Observed and CTL-modelled PW fields

Figures 3 and 4 show the MODIS-observed and UM-CTL-modelled PW fields and their components at 1020 UTC 27 July 2005 respectively. Comparison of the observed and modelled pairs indicates that:

(1) There is a slight wet bias on the western edge of the volcano and an obvious dry bias over the Etna summit in the modelled full PW field relative to the observations (Figs. 3a and 4a). Otherwise, the observed PW pattern, including the strong correlation between the PW and the surface elevation and the asymmetric gradients over the eastern and western slopes, which are partly due to the different elevation gradients over these slopes, are satisfactorily simulated. The MODIS values are, on average, only 0.3 mm wetter than those of the UM, the root mean

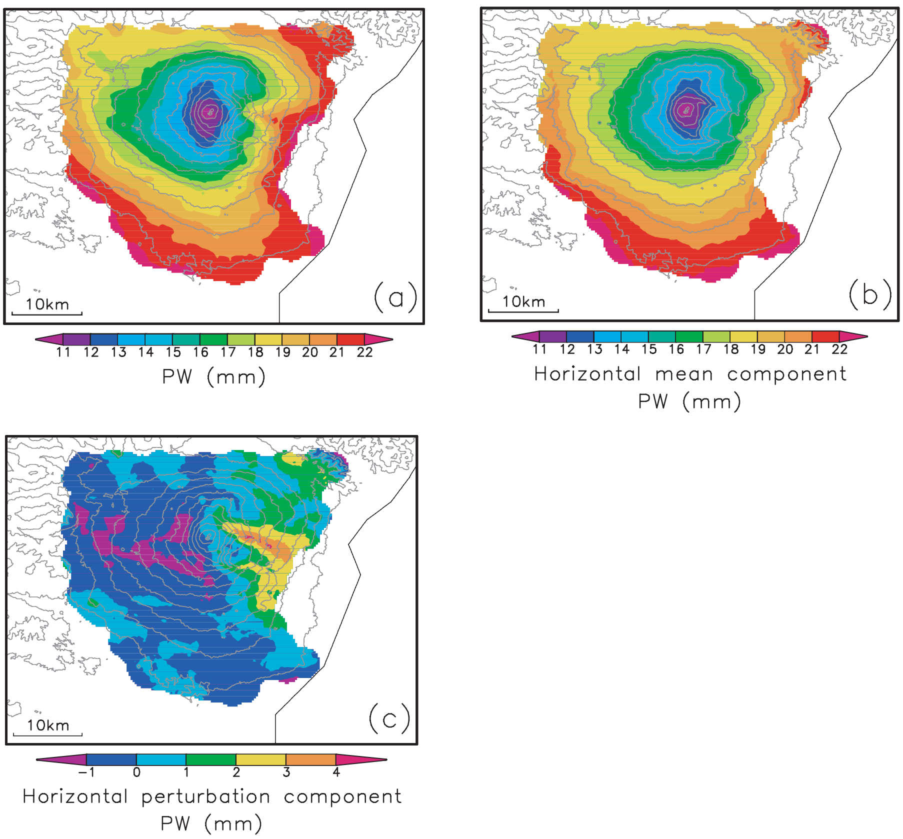

Fig. 3. MODIS-observed full PW field (a), horizontal mean component (b), and horizontal perturbation component (c), over Etna at 1020 UTC 27 July 2005.

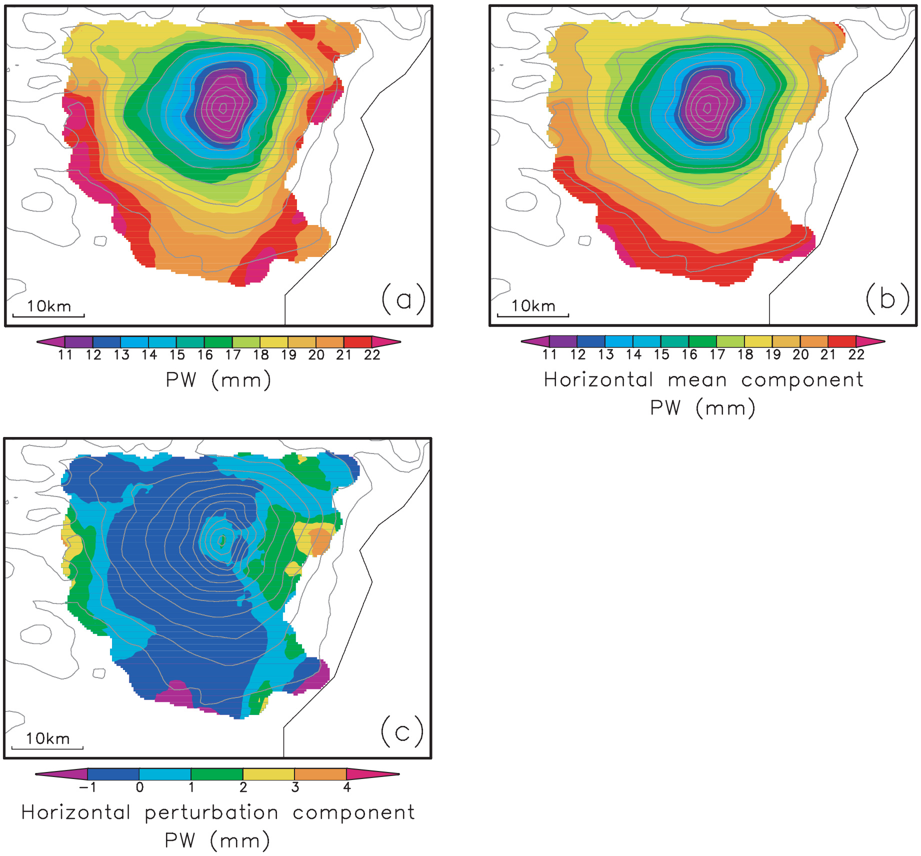

Fig. 4. UM CTL-modelled full PW field (a), horizontal mean component (b), and horizontal perturbation component (c), over Etna at 1020 UTC 27 July 2005.

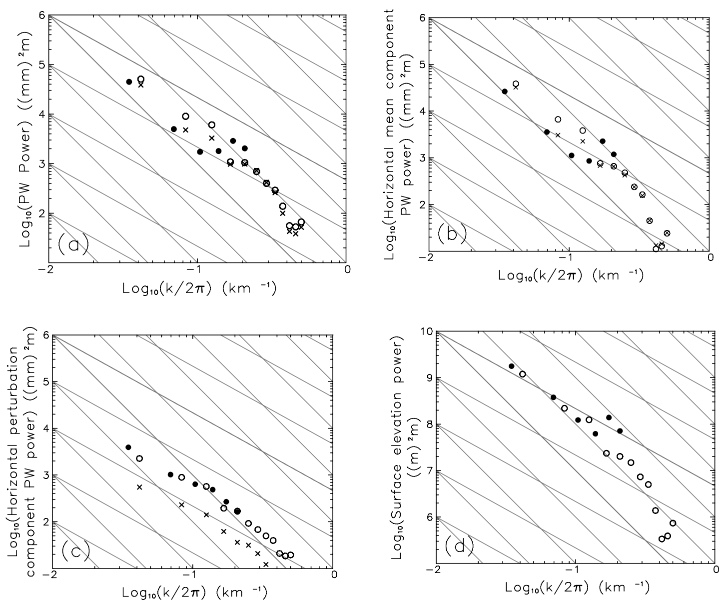

Fig. 5. Discrete power spectra of observed (closed circle) and modelled (CTL: open circle, NSR: cross) full PW field (a), horizontal mean component (b), horizontal perturbation component (c) and surface elevation (d). The two sets of grey lines have slopes of –3 and –5/3.

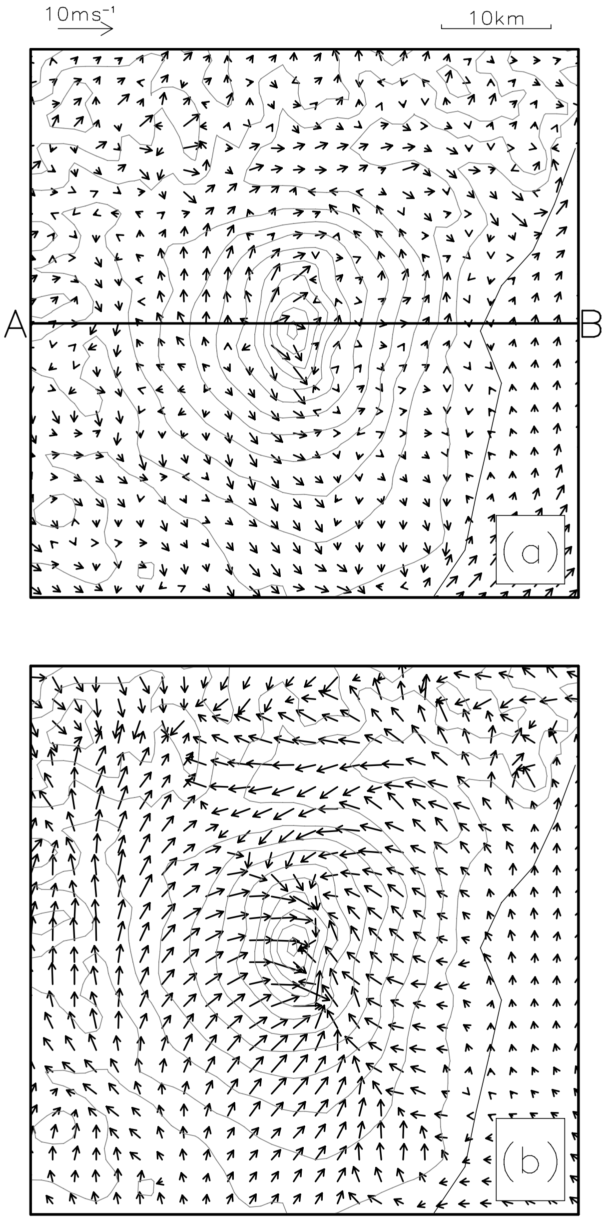

Fig. 6. (a) NSR- and (b) CTL-simulated 10 m wind fields at 1020 UTC 27 July 2005. AB is the W–E cross-section through the summit used in Fig. 7.

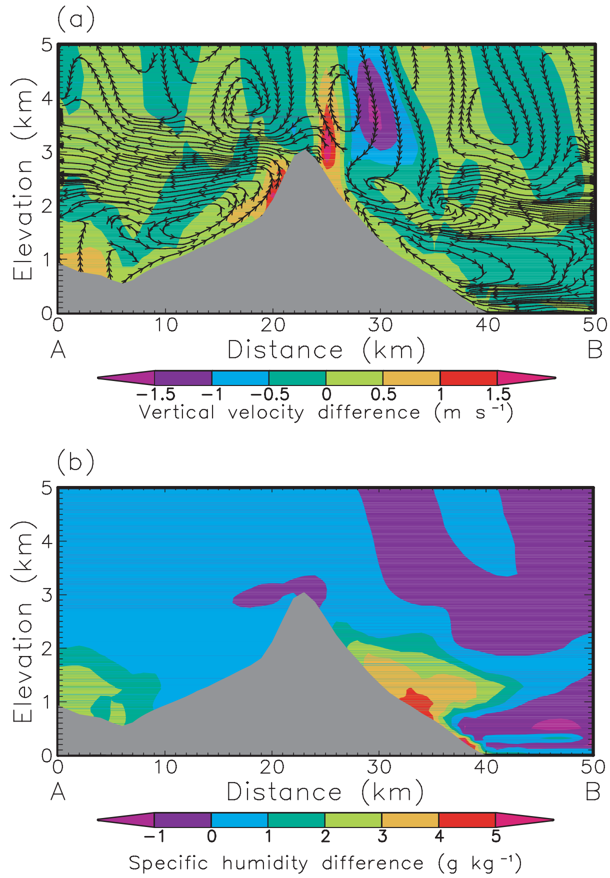

Fig. 7. (a) Differences in the wind (streamline) and vertical velocity (colour shaded, positive up, ms^{-1}); (b) differences in specific humidity ($g\ kg^{-1}$), between the CTL and NSR simulations along the section AB.

square difference between the two is 1.3 mm, and the correlation coefficient is 0.93.

(2) The contours of the horizontal mean components of the PW fields, as expected, follow the orographic contours (Fig. 3b and 4b). The model error is shown more clearly in Fig. 2. Below 1500 m a.s.l. (above sea level), the modelled curve follows the observations quite well. Over 2000 m a.s.l., the model becomes drier, which is consistent with the dry bias seen in the modelled full PW fields. This model weakness may reflect the errors in the initial humidity fields upstream of the Etna mountain.

(3) The observed horizontal perturbation component of the PW field (Fig. 3c) shows a broad low on the western slopes of the volcano trending North Northwest. The eastern and northeastern slopes are positive with a distinct ridge of elevated values extending from the East Southeast on the north side of the Valle del Bove (Fig. 1). There is no MODIS coverage of the lower eastern slopes. Both these main observed features are also shown by the model (Fig. 4c), though the ridge feature is less obvious.

3.2. *Power spectra of the surface elevation and PW fields*

The full (Fig. 5a) and horizontal mean component (Fig. 5b) PW fields for both the observations and the model show a similar spectral structure to that of the surface elevation (Fig. 5d) (the slope is around -3 at wavelengths greater than 10 km). Because Etna is an isolated mountain, its surface elevation power spectrum may not necessarily follow a k^{-2} behaviour, which is the general case for the Earth's topography (Balmino, 1993). The observed and modelled horizontal perturbation component PW field both show a spectral structure with a slope of $-\frac{5}{3}$, consistent with that for wind, temperature and humidity at mesoscale

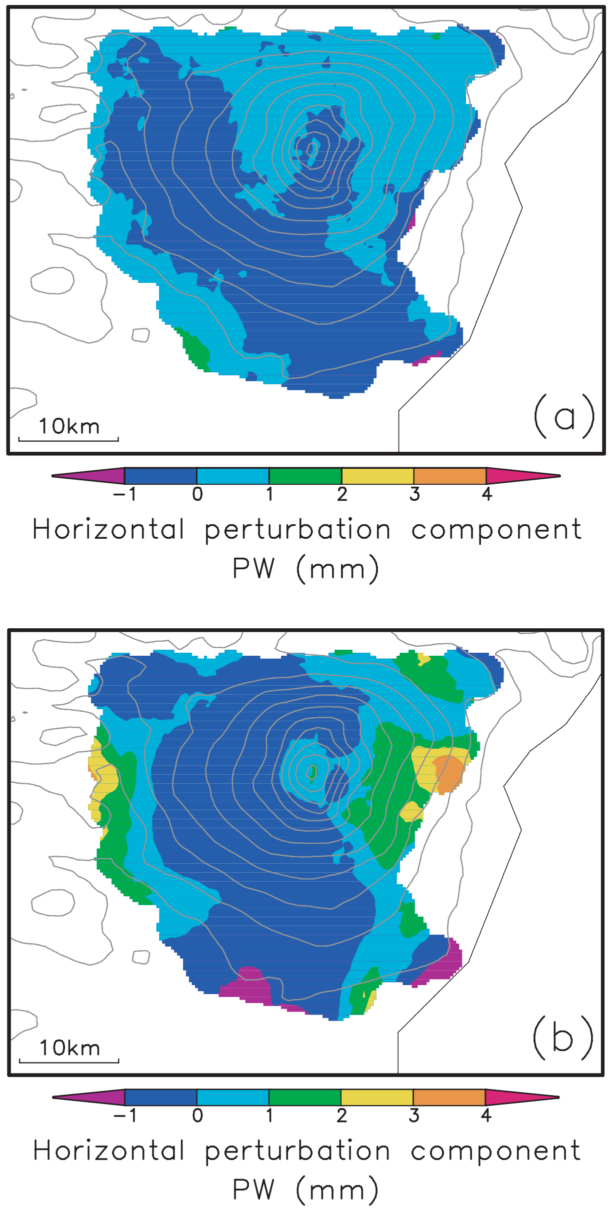

Fig. 8. Horizontal perturbation component of the PW field over Etna at 1020 UTC 27 July 2005 simulated by the UM NSR (a), and UM CTL (b).

(Nastrom and Gage, 1985; Cho et al., 1999; Koshyk et al., 1999).

3.3. Sea breeze mechanism

The character of the horizontal perturbation component of the PW field suggests that the long wavelength feature to the west may be related to a synoptic scale system, while the higher amplitude feature to the east derives from a more local mechanism. The timing (1020 UTC on a clear summer day) and location (near the coast) of the eastern PW feature suggests a possible

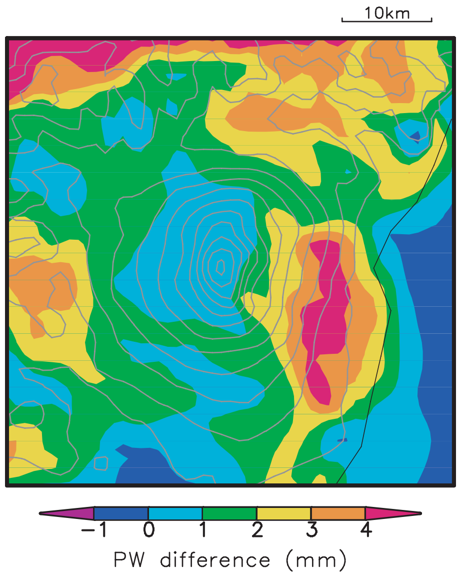

Fig. 9. PW difference between CTL and NSR simulations at 1020 UTC 27 July 2005.

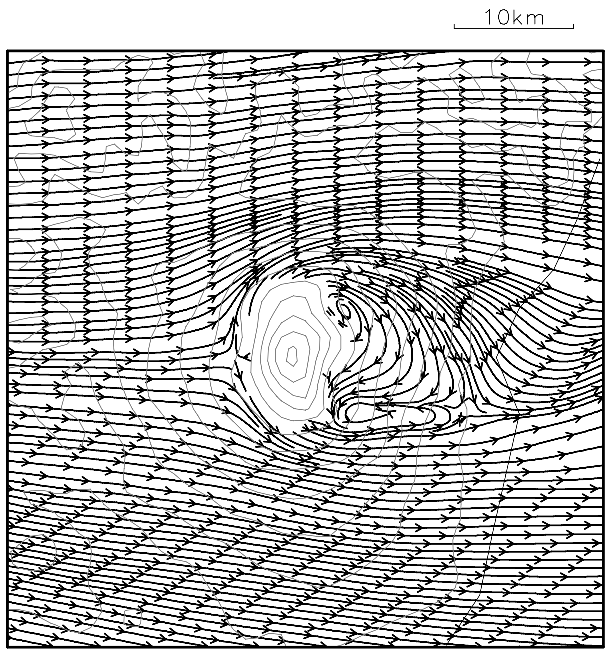

Fig. 10. NSR simulated wind at 2000 m a.s.l. at 1020 UTC 27 July 2005.

sea breeze effect. To test this idea we undertook an experiment (NSR) in which the solar radiation scheme was removed, while other physical processes were kept the same as in the CTL forecast.

Figure 6 shows the CTL- and NSR-simulated wind at 10 m altitude at 1030 UTC 27 July 2005. Without solar heating, the NSR result shows weak downslope surface winds in the late morning. In contrast, strong sea breezes from SE to NW and

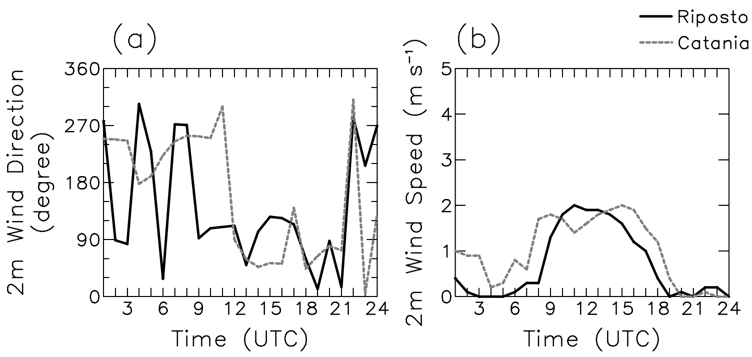

Fig. 11. Observed temporal variation of 2 m altitude wind direction (a), and speed (b) at Riposto (solid line) and Catania (dashed line) on 27 July 2005.

anabatic winds are stimulated by solar heating in the CTL simulation. More specifically, after sunrise (0400 UTC), the CTL results show that heating over the land surface begins to generate slope breezes on all sides of the volcano. Later on, at about 0800 UTC, the soil becomes warmer and a convective regime is established replacing the nocturnal stable regime, which still persists in the NSR result. On the volcano's eastern lower slopes, the sea breeze penetrates inland, where it is reinforced by the slope flow directed towards the top of the volcano. A vertical velocity wind dipole forms near the summit of the volcano (Fig. 7a) and returning currents occur in opposite directions, at 2–4 km altitude. This sea breeze behaviour is consistent with Favalli et al.'s results for another case study on Etna (Favalli et al., 2004). Consequently, there is more marine moisture brought in by the sea breeze in the CTL forecast than that in NSR experiment over the mountain's eastern slope (Fig. 7b). The horizontal perturbation component PW field from the NSR experiment shows no sign of the strong West Northwest–East Southeast moisture gradient due to the lack of the sea breeze intrusion (Fig. 8a), whereas the CTL forecast captured this gradient successfully (Fig. 8b). The increase in PW due to sea breeze intrusion can reach as high as 4–5 mm (Fig. 9), which is consistent with Bastin et al.'s sea breeze case study in southeastern France using GPS observations (Bastin et al., 2005). Without sea breeze intrusion, the power spectral energy of the horizontal perturbation component PW field for the NSR experiment is much lower than that for the observations and CTL forecast (Fig. 5c). This is because solar heating in the presence of orography and a land/sea contrast drives circulations that advect water vapour into the domain in complex ways that boost the PW power spectrum at the mesocale range of the wavelengths shown. Even without a solar radiation scheme, the low-amplitude western feature seen in the MODIS-observed and UM CTL-modelled horizontal perturbation component PW field maps is still present in the NSR map (Fig. 8a). This feature may be a synoptic feature due to the advection of dry and warm air by low level southwest flow from Africa (ECMWF PW analysis at 1200 UTC, not shown).

Figure 10 shows the lower tropospheric wind at 2000 m a.s.l. from the NSR experiment. The flow is characterized by strong streamline splitting around the mountain with the formation of a well-defined asymmetric vortex pair in the wake of the mountain. The flow is essentially restricted to horizontal planes, except in two layers near the surface and the mountain peak. This generally agrees with the results from idealised experiments (Miranda and James, 1992). Such low Froude number flow (∼0.2) is in contrast to the much higher Froude number case example used by Wadge et al. (2002) in which flow over the mountain's summit dominated behaviour.

Figure 9 shows a clear spatial inhomogeneity of the sea breeze intrusion. To the south, over Catania, there was no sign of sea breeze penetration while further north, near Riposto (Fig. 1), the sea breeze can penetrate far inland. This is because differential heating of land and water, differential heating between air next to the slope and air at the same level farther from the slope and the disturbance of stratified larger-scale flow over the mountain, reinforce each other to lower the pressure on the eastern side of the mountain, which drives air from over the ocean farther inland in the lee of the mountain than the sea breeze would normally penetrate by itself. On the south side of the mountain, the relative lack of penetration of the sea breeze is due to the interaction between the low level ambient wind (WSW flow) and the sea breeze, and the weaker onshore pressure gradient compared with that on the eastern (lee) side of the mountain.

This is confirmed by the observations. Figure 11 shows that the observed sea breeze passed Riposto at about 0900 UTC, 3 hours earlier than it did near Catania.

4. Conclusions

Our method of decomposing the PW field over Etna for 27 July 2005 into horizontal mean and horizontal perturbation components has been demonstrated for both remotely sensed (MODIS) and forecast model (UM) data. Power spectral analysis shows that the PW decomposition is reasonable and practical. The full and horizontal mean component PW power spectra are similar to that of the orography. The horizontal perturbation PW component shows a wave number dependence of $k^{-\frac{5}{3}}$ in the mesoscale range. The current state-of-the-art forecast model can reproduce most of the observed PW structure. By switching off the solar radiative forcing in the forecast model we show that much of the horizontal perturbation component of the PW field on the seaward side of the volcano was probably produced by the combined effect of land-sea and upslope breezes during the morning. It has been observed that the ground motion signals detected by DInSAR from mid-morning acquisitions tend to be noisier because they are more affected by greater path delays (more variability of water vapour content) than those acquired at night (Massonnet and Feigl, 1998). Our work demonstrates one specific mechanism by which this can be explained. As a result extra care is required with daytime DInSAR data over mountains next to the sea.

5. Acknowledgments

This work was funded by NERC grant NER/A/S/2003/00470. The manuscript benefited from constructive reviews by D. Dempsey and an anonymous reviewer.

References

Avara, P., Kays, M. 1971. The effect of interpolation of data upon the harmonic coefficients. *ECOM, 5354*, Defense Technical Information Center, 33 pp.

Baines, P. G. 1995. *Topographic effects in stratified flows*, Cambridge University Press, Cambridge, 482 pp.

Balmino, G. 1993. The spectra of the topography of the Earth, Venus and Mars. *Geophys. Res. Lett.* **20**, 1063–1066.

Bastin, S., Champollion, C., Bock, O., Drobinski, P. 2005. On the use of GPS tomography to investigate water vapour variability during a Mistral/sea breeze event in southeastern France. *Geophys. Res. Lett.* **32**, L05808, doi: 10.1029/2004GL021907.

Cho, J. Y. N., Zhu, Y., Newell, R. E., Anderson, B. E., Barrick, J. D. and co-authors. 1999. Horizontal wavenumber spectra of winds, temperature and trace gases during the Pacific Exploratory Missions: 1. Climatology. *J. Geophys. Res.* **104**(D5), 5697–5716.

Favalli, M., Mazzarini, F., Pareschi, M. T. and Boschi, E. 2004. Role of local wind circulation in plume monitoring at Mt. Etna volcano (Sicily): Insights from a mesoscale numerical model. *Geophys. Res. Lett.* **31**, L09105, doi:10.1029/2003GL019281.

Foster, J. and Bevis, M. 2003. Lognormal distribution of precipitable water in Hawaii. *Geochem. Geophys. Geosys.* **4**(7), 1065, doi;10.1029/2002GC000478.

Hanssen, R. 2001. *Radar interferometry data interpretation and data analysis*, Kluwer Academic, Dordrecht, 308 pp.

Koshyk, J. N., Boville, B. A., Hamilton, K., Manzini, E. and Shibata, K. 1999. Kinetic energy spectrum of horizontal motions in middle-atmosphere models. *J. Geophys. Res.* **104**, 27177–27190.

Kuo, Y.-H., Zou, X. and Guo, Y.-R. 1996. Variational assimilation of precipitable water using a nonhydrostatic mesoscale adjoint model. Part I: Moisture retrieval and sensitivity experiment. *Mon. Weather Rev.* **124**, 122–147.

Li, Z., Muller, J.-P., Cross, P. and Fielding, E. J. 2005. Interferometric synthetic aperture radar (InSAR) atmospheric correction: GPS, Moderate Resolution Imaging Spectroradiometer (MODIS) and InSAR integration. *J. Geophys. Res.* **110**(B3), B03410, doi:10.1029/2004JB003446.

Met Office 2004 "Unified Model User Guide", Available online at: http://www.cgam.nerc.ac.uk/um/docs/

Massonnet, D. and Feigl, K. L. 1998. Radar interferometry and its application to changes in the Earth's surface. *Rev. Geophys.* **36**(4), 441–500.

Miranda, P. M. A. and James, I. N. 1992. Non-linear three-dimensional effects on gravity-wave drag: Splitting flow and breaking waves. *Q. J. R. Meteorol. Soc.* **118**, 1057–1081.

Nastrom, G. D. and Gage, K. S. 1985. A climatology of atmospheric wavenumber spectra of wind and temperature observed by commercial aircraft. *J. Atmos. Sci.* **42**(9), 950–960.

Remy, D., Bonvalot, S., Briole, P. and Murakami, M. 2003. Accurate measurements of tropospheric effects in volcanic areas from SAR interferometry data: Application to Sakurajima volcano (Japan). *Earth Planet. Sci. Lett.* **67**(30), 1–12.

Rotunno, R. and Ferretti, R. 2001. Mechanisms of intense Alpine rainfall. *J. Atmos. Sci.* **38**, 1732–1749.

Skamarock, W. C. 2004. Evaluating mesoscale NWP models using kinetic energy spectra. *Mon. Wea. Rev.* **132**, 3019–3032.

Trenberth, E., Fasullo, J. and Smith, L. 2005. Trends and variability in column-integrated atmospheric water vapour. *Climate Dynam.* **24**, 741–758, DOI 10.1007/s0038-005-0017-4.

Wadge, G., Webley, P. W., James, I. N., Bingley, R., Dodson, A. and co-authors. 2002. Atmospheric models, GPS and InSAR measurements of the tropospheric water vapour field over Mount Etna. *Geophys. Res. Lett.* **29**(19), 1905, doi:10.1029/2002GL015159.

Zhu, M., Wadge, G., Holley, R. J., James, I. N., Clark, P. A. and co-authors. 2007. High resolution forecast models of water vapor over mountains: comparison with MERIS and Meteosat data. *Geosc. Rem. Sens. Lett.* **4**(3), 401–405.